Jing *et al. Microstructures* **2025**, *5*, 2025047
DOI: 10.20517/microstructures.2024.149

Microstructures

Research Article

Open Access

Check for updates

Reversible phase transitions and enhanced electrostrain in BNST-*x*FN ceramics under electric and thermal stimuli

Ruiyi Jing, Wanchang Man, Xinru Nie, Leiyang Zhang, Li Jin

Electronic Materials Research Laboratory, Key Laboratory of the Ministry of Education, School of Electronic Science and Engineering, Faculty of Electronic and Information Engineering, Xi'an Jiaotong University, Xi'an 710049, Shaanxi, China.

Correspondence to: Dr. Ruiyi Jing, Electronic Materials Research Laboratory, Key Laboratory of the Ministry of Education, School of Electronic Science and Engineering, Faculty of Electronic and Information Engineering, Xi'an Jiaotong University, No. 28, Xianning West Road, Xi'an 710049, Shaanxi, China. E-mail: ryjing@xjtu.edu.cn; Prof. Li Jin, Electronic Materials Research Laboratory, Key Laboratory of the Ministry of Education, School of Electronic Science and Engineering, Faculty of Electronic and Information Engineering, Xi'an Jiaotong University, No. 28, Xianning West Road, Xi'an 710049, Shaanxi, China. E-mail: ljin@mail.xjtu.edu.cn

How to cite this article: Jing, R.; Man, W.; Nie, X.; Zhang, L.; Jin, L. Reversible phase transitions and enhanced electrostrain in BNST-*x*FN ceramics under electric and thermal stimuli. *Microstructures* **2025**, *5*, 2025047. https://dx.doi.org/10.20517/microstructures.2024.149

Received: 6 Dec 2024 **First Decision:** 16 Jan 2025 **Revised:** 14 Feb 2025 **Accepted:** 25 Feb 2025 **Published:** 17 Apr 2025

Academic Editors: Xiaozhou Liao, Shiqing Deng **Copy Editor:** Fangling Lan **Production Editor:** Fangling Lan

Abstract

Ferroelectric materials based on $(Bi_{0.5}Na_{0.5})TiO_3$ are well-known for their outstanding chemical stability and exceptional electrical properties, particularly their large electrostrain response under applied electric fields, positioning them as promising candidates for precision actuator applications. In this study, we investigate the electrical and structural responses of lead-free $(Bi_{0.38}Na_{0.38}Sr_{0.24})Ti_{1-x}(Fe_{0.5}Nb_{0.5})_xO_3$ (BNST-*x*FN) ferroelectric ceramics under the combined effects of temperature and electric field. Using *in-situ* electric field and variable-temperature Raman spectroscopy, piezoelectric force microscopy, and comprehensive dielectric and ferroelectric property evaluations, we explore the evolution of structural transformations, polarization behavior, and macroscopic property changes in ceramics with different initial phase structures under thermal and electrical stimuli. Notably, the BNST-0.01FN composition, located near the boundary between the non-ergodic relaxor and ergodic relaxor phases, exhibits a remarkable room-temperature electrostrain of 0.37%, driven by a reversible electric field-induced nonpolar-to-polar phase transition. Upon heating, as the BNST ceramic approaches the phase boundary, a prominent electrostrain (~0.38%) is observed near the temperature of the ferroelectric-to-relaxor phase transition (T_{FR}, ~60 °C) under the electric field. This study combines *in-situ* microstructural analysis with

macroscopic ferroelectric characterization, providing a deeper understanding of the dynamic coupling between microscopic fields and macroscopic electrical properties, and offering valuable insights for the design of high-performance lead-free ferroelectric ceramics.

Keywords: $(Bi_{0.5}Na_{0.5})TiO_3$, relaxor, phase boundary, electrostrain, reversible phase transition

INTRODUCTION

Ferroelectric materials have long been at the forefront of materials science due to their unique electromechanical coupling properties, which enable a wide range of applications in sensors, actuators, and storage devices[1-5]. Among these, multilayer ceramic actuators (MLCAs) based on ferroelectric ceramics exhibit electric-field-induced strain (electrostrain) with numerous advantages, including high precision, rapid response, and low power consumption, making them ideal for ultra-precise positioning, as well as micro- and nano-scale actuation and control[6-8]. These attributes underscore their significant potential in advanced technological applications. Currently, commercially available actuators, such as fuel injection valves and micro-positioning systems, are typically based on lead-based ferroelectric materials such as lead zirconate titanate [$Pb(Zr,Ti)O_3$ (PZT)] and its solid solutions[9-11]. However, the toxic lead oxides used in these materials pose serious health risks, driving the urgent need for effective lead-free alternatives[12-14].

The discovery of large electrostrain properties in $(Bi_{0.5}Na_{0.5})TiO_3$-$BaTiO_3$-$(K_{0.5}Na_{0.5})NbO_3$ (BNT-BT-KNN) materials by Zhang *et al.* in 2007[15] marked a significant breakthrough, attracting considerable attention to BNT and its solid solutions, which exhibit recoverable electrostrain that comparable, and even surpass, those of lead-based materials[7,16,17]. This breakthrough opened new avenues for the development of lead-free ferroelectric actuators, with the potential to replace lead-based materials in commercial applications, spurring extensive research in this area[18,19]. For instance, BNT-BT-$K_{0.47}Na_{0.47}Li_{0.06}Nb_{0.99}Sb_{0.01}O_{2.99}$ (BNBT-KNLNS) ceramics, designed by Li *et al.*, exhibited large electrostrain values (0.32%-0.51%) and low strain hysteresis (~11.1%) across a wide temperature range (25-125 °C)[20]. This exceptional performance is attributed to the incorporation of a small fraction of ferroelectric states within the morphotropic phase boundary (MPB) matrix, which consists of tetragonal (T) and rhombohedral (R) phases, enabling a reversible transition from the relaxor to the ferroelectric phase[21].

These findings underscore the significant impact of phase transitions on the electrostrain properties of BNT-based materials, highlighting the close relationship between electrostrain behavior and phase boundary characteristics. In these materials, the relaxor phases can be classified as the non-ergodic relaxor (NER) and ER phases, with the key distinction being whether the ferroelectric phase can be stabilized after the electric field is removed[22]. The phase boundaries in BNT-based materials are often optimized through the formation of solid solutions or the introduction of dopant components, which further enhance their electrostrain performance[17].

BNT-based actuator materials, driven by phase-transition electrostrain properties, are often plagued by significant hysteresis and high driving electric fields, which remain major obstacles to their practical application[7]. However, doping with ferroelectric materials such as $BaTiO_3$ (BT) and paraelectric materials such as $SrTiO_3$ (ST) with lower coercive fields has proven effective in reducing both the driving electric field and strain hysteresis, facilitating high electrostrain responses[23,24]. For instance, Bai *et al.* demonstrated that the incorporation of ST into BNT-0.17$(Bi_{0.5}K_{0.5})TiO_3$ (BNT-0.17BKT) ceramics enhanced electrostrain while simultaneously decreasing ferroelectricity. At a relatively low driving electric field of 60 kV/cm, these ceramics exhibited a substantial electrostrain response (S = 0.38%, d^*_{33} ~ 626 pm/V)[25]. Similarly, Wang *et al.*

reported that the addition of ST to the BNT-BT ceramic system enabled high electrostrain at a lower driving field of 40 kV/cm (S = 0.2%, d^*_{33} ~ 490 pm/V)[26]. In the BNT-ST system, Lalitha *et al.* observed that the phase transition between the relaxor and ferroelectric phases occurred spontaneously with an increased ST content, even in the absence of an applied external electric field, ultimately achieving a large electrostrain value of 0.52% at 60 kV/cm[27]. The design and development of BNT-ST-based solid solution ceramics has thus provided a promising direction for the advancement of lead-free actuator materials.

In addition to the incorporation of new components and BNT-based solid solution strategies, ceramics can also be modified through ion doping, where ions of varying valences, radii, and concentrations are introduced into the ceramic matrix to induce lattice distortion, oxygen vacancies, and localized random fields, thereby enhancing the electromechanical properties[1-7]. Ion doping can be categorized based on the doping site: A-site[28], B-site[29,30], and A/B-site co-doping[31-34]. Multiple-ion doping can optimize the electric domain structure and phase transition behavior, reducing hysteresis and driving electric fields while improving electrostrain responses. For example, Rahman *et al.* achieved an electrostrain of 0.38% at 70 kV/cm by doping Ba^{2+} and Zr^{4+} into BNT-BT[35]. Notably, when doping at the B-site, the use of composite ions has been shown to be more effective than single-ion doping. Cheng *et al.* introduced the composite ion $(Fe_{0.5}Nb_{0.5})^{4+}$ into the BNT-BT system, achieving a significant electrostrain of 0.42% at 50 kV/cm[36]. Similarly, Bafandeh *et al.* demonstrated that doping Ga^{3+} and Ta^{5+} into BNT resulted in an electrostrain of 0.4% at 60 kV/cm[37]. Other common B-site composite ions include $(Zn_{1/3}Nb_{2/3})^{4+}$[30], $(Mn_{0.5}Sb_{0.5})^{4+}$[38], $(Fe_{0.5}Ta_{0.5})^{4+}$[39], and so on. In summary, B-site composite ion doping offers a promising approach for enhancing electrostrain performance in BNT-based materials. By carefully controlling the types and ratios of dopant ions, it is possible to finely tune the electric domain structure and phase transition properties, achieving high electrostrain responses and low hysteresis at reduced electric fields. This strategy not only improves the electromechanical performance of the material but also enhances its reliability and stability in practical applications, thus providing a new pathway for the development of lead-free actuator materials.

The electrostrain response of BNT-based ceramics is intrinsically linked to their complex phase transitions, which are highly sensitive to both thermal and electrical stimuli. However, the interplay between temperature and electric field, along with its influence on the electrostrain response, remains not fully understood. Identifying the relationship between microstructure, polarization behavior, and macroscopic electrostrain is crucial for elucidating the underlying mechanisms. *In-situ* Raman spectroscopy, a powerful tool for probing local structural changes in ferroelectric materials under varying temperature and electric field conditions, offers real-time insights into the material's response to external stimuli. This provides valuable information on the atomic-scale mechanisms that govern the macroscopic properties of these materials[40]. Additionally, piezoelectric force microscopy (PFM) is an essential technique for direct observation of domain structures and polarization responses in ferroelectric ceramics[41]. Combining these techniques with measurements of the temperature-dependent properties of ceramics, such as dielectric behavior and polarization-electric field (*P-E*) hysteresis loops- represents a reliable method for characterizing the electromechanical properties of BNT-based materials[42]. This integrated approach enables a comprehensive understanding of the electrostrain response in BNT-based ceramics, which is critical for their application in high-precision positioning systems and sensors.

This study investigates the electrostrain response of BNT-based ceramics under dual stimulation by temperature and electric field, with a focus on structural distortions, local polarization behavior, and their effects on electrostrain. The work was conducted on $(Fe_{0.5}Nb_{0.5})^{4+}$-doped BNT-0.24ST systems, featuring different initial phase structures with different doping levels. An electrostrain of 0.37% was achieved in ceramics with 0.01 mol.% $(Fe_{0.5}Nb_{0.5})^{4+}$ doping. Notably, around 60 °C, BNT-0.24ST ceramics undergo a

NER to ER phase transition, leading to a significant electrostrain (~0.38%) via a reversible nonpolar-to-polar phase transition induced by the electric field. The intrinsic mechanism behind this electrostrain enhancement is explored through a comprehensive analysis of *in-situ* electric field Raman spectroscopy, PFM, and ferroelectric properties (*P-E* loops, *S-E* curves and *J-E* curves) across varying electric fields and temperatures. Our findings not only illuminate the complex phase transitions in BNT-based ceramics but also offer valuable insights for the design of high-performance, lead-free ferroelectric ceramics for actuator applications.

MATERIALS AND METHODS

Ceramic samples of the $(Bi_{0.38}Na_{0.38}Sr_{0.24})Ti_{1-x}(Fe_{0.5}Nb_{0.5})_xO_3$ (BNST-*x*FN, x = 0, 0.01, 0.02, 0.03) system were synthesized using a traditional solid-state reaction method. The raw materials, including Bi_2O_3 (99%), Na_2CO_3 (99.8%), $SrCO_3$ (99%), TiO_2 (98%), Fe_2O_3 (99%) and Nb_2O_5 (99.99%), were supplied by Sinopharm Chemical Reagent Co. Ltd. (China). Prior to mixing, all materials were dried at 100 °C for over 24 h to ensure the accuracy of doping content. The components were then thoroughly mixed by ball milling for 6 h at a rotational speed of 300 rpm. The ball-to-powder weight ratio was maintained at 10:1 to ensure effective mixing. The well-mixed slurry was dried, and the resulting powder was transferred to an alumina crucible and calcined in a muffle furnace. The calcination process was conducted at 850 °C for 3 h with a heating rate of 3 °C/min. The calcined powder was further milled for 24 h at a rotational speed of 300 rpm to refine the powder and enhance its fluidity during subsequent sintering. Isostatic pressing, without the addition of a polyvinyl alcohol binder to avoid porosity from binder removal, was used to form discs with a diameter of 10 mm and a thickness of approximately 1.5 mm. To prevent the volatilization of Na and Bi elements during the sintering process, which can lead to compositional inhomogeneity and defects, a burial sintering method was employed. The green bodies were placed in an alumina crucible and surrounded by the same composition of calcined powder. The crucible was then sealed to create a closed environment. The ceramics were sintered at 1,080-1,130 °C for 2 h with a temperature ramp rate of 3 °C/min to form high-quality ceramic samples.

For X-ray diffraction (XRD) measurements, ceramic samples were milled to fine powder using an onyx mortar and annealed at 500 °C for several hours to remove internal stresses. XRD was performed using a SmartLab X-ray diffractometer (Rigaku, Japan) equipped with a temperature control system. Scans were conducted over a range of 10° to 90° at room temperature (RT), with a step size of 0.01° and a scan rate of 1°/min. Data refinement was performed using the FULLPROF software (version 2000) to accurately determine the lattice parameters. High-temperature XRD tests were conducted on both poled and unpoled bulk ceramics. The samples were polished, annealed, and then covered with room-temperature silver paste, followed by polarization for over 20 min at an electric field higher than the coercive field. The silver paste was subsequently removed with alcohol. Test data is collected at 10 °C intervals, with the temperature rising at a rate of 10 °C/min, with testing commencing after stabilization at the target temperature for 1 min, using a scanning step of 0.01° and a rate of 1°/min. Raman spectra were collected using a Raman spectrometer (LabRam HR Evolution, HORIBA JOBIN YVON, France) equipped with a heating stage and excited by a 532 nm laser. *In-situ* Raman measurements were performed under an applied electric field, with silver paste electrodes on both the upper and lower surfaces of the side-polished ceramic samples. The temperature was ramped at 10 °C/min, with measurements taken after stabilization at the target temperature for 1 min. Micro-morphological images were obtained by thermally etching the polished samples for 20 min at approximately 100 °C below the sintering temperature, followed by scanning electron microscopy (SEM, Quanta FEG 250, FEI, USA). Dielectric properties were measured on silver-electrode-coated samples using a multi-frequency LCR meter (E4980A, Agilent, USA). Additionally, the temperature rises from RT to 450 °C at a rate of 3 °C per minute, and the data is captured once every one degree of temperature rises. The

ferroelectric properties, including *P-E* loops, *S-E* curves and *J-E* curves, were obtained using a ferroelectric workstation (TF analyzer 2000, aixACCT, Germany) equipped with a temperature control system and a laser interferometer vibrometer (SP-S 120, SIOS Meβtechnik GmbH, Germany). For the ferroelectric measurements, gold (Au) electrodes were sputtered onto the polished surfaces of the ceramic samples. The sputtering process was performed under the following conditions: the Au electrodes were sputtered for a duration of 4 min at a current of 30 mA, with an electrode area of 3.14 mm^2. When acquiring variable-temperature data, it is crucial to allow the set temperature to be reached and stabilized for a duration of 2 min prior to commencing data collection. The ferroelectric domain structures of the samples were observed using an atomic force microscope (AFM, Dimension Icon, Bruker, USA) in PFM mode. The probe we employed is the MESP mode tip configuration. The probe material is n-type antimony-doped Si with a resistivity of 0.01-0.025 Ω cm. Prior to PFM testing, the surface of the sample was polished using a diamond suspension without additional heat treatment.

RESULTS AND DISCUSSION

In Figure 1A, the XRD patterns of BNST-*x*FN ceramics reveal that both BNST and BNST-0.01FN exhibit a pure perovskite structure within the resolution range of the instrument. And it can be seen from Figure 1B that the (110) diffraction peak shifts to higher angles with increasing doping content, a result of the substitution of Ti^{4+} by the $(Fe_{0.5}Nb_{0.5})^{4+}$ composite ion at the B-site. In ABO_3-type perovskites, the B-site coordination number (CN) is 6, with an ion radius of 0.605 Å[43] for Ti^{4+}. For Fe^{3+} and Nb^{5+}, which have the same CN, the ion radii are 0.55 and 0.645 Å, respectively. The calculated ion radius of $(Fe_{0.5}Nb_{0.5})^{4+}$ is 0.595 Å, slightly smaller than that of Ti^{4+}, resulting in the observed peak shift to higher angles according to Bragg's Law ($2d\sin\theta = n\lambda$)[21,43]. Notably, for doping levels of 0.02 and above, the XRD patterns show a second-phase peak near 30°, along with additional peaks indicative of a secondary phase, $Bi_5Ti_3FeO_{15}$ (PDF No. 89-8545), as seen in Figure 1B and C. To further elucidate the phase structure, we refined the XRD patterns, with the results and refined parameters shown in Supplementary Figure 1 and Supplementary Table 1. The refinement reveals that BNST and BNST-0.01FN exhibit a mixed-phase structure, consisting of R (space group *R3c*) and T (space group *P4bm*) phases. In contrast, BNST-0.02FN and BNST-0.03FN contain $Bi_5Ti_3FeO_{15}$ in addition to the perovskite phases. Removing the effect of the impurity phase, the T phase content increases with doping, indicating a phase transition from the NER phase to the ER phase as expected.

Raman spectroscopy, a powerful vibrational technique, provides valuable insights into the molecular vibrational modes and structural evolution of materials[40,44-46]. We measured the Raman spectra of BNST-*x*FN ceramics in the wavenumber range of 20-1,000 cm^{-1}, with the results shown in Figure 1D. The Raman spectra can be divided into four distinct regions[40,44], each corresponding to different lattice vibrational modes. Region I (wavenumbers below ~200 cm^{-1}) is primarily associated with vibrations of the A-site cations, such as Na^+, Bi^{3+}, and Sr^{2+}, in this study. Region II, spanning roughly 200-425 cm^{-1}, is linked to the vibrational modes of the Ti-O bond. The region from 425 to 680 cm^{-1} corresponds to vibrations of the TiO_6 octahedron, including stretching and bending modes of the oxygen octahedra. In Region IV (above 680 cm^{-1}), the vibrational modes are primarily attributed to A_1 and E (longitudinal optical, LO) modes[47]. Previous studies on the Raman spectra of perovskite materials suggest that *R3c* and *P4bm* phases could have up to 24 and 28 Raman-active modes, respectively[40].

However, due to the relative weakness of some modes[48], we used 13 Gaussian-Lorentzian peak functions to deconvolve the Raman spectra of BNST, BNST-0.01FN, BNST-0.02FN, and BNST-0.03FN, employing the best fitting algorithm, as shown in Figure 1D. The fitted peak positions are summarized in Figure 1E. Comparing the four Raman spectra in Figure 1D, it is evident that BNST and BNST-0.01FN exhibit similar

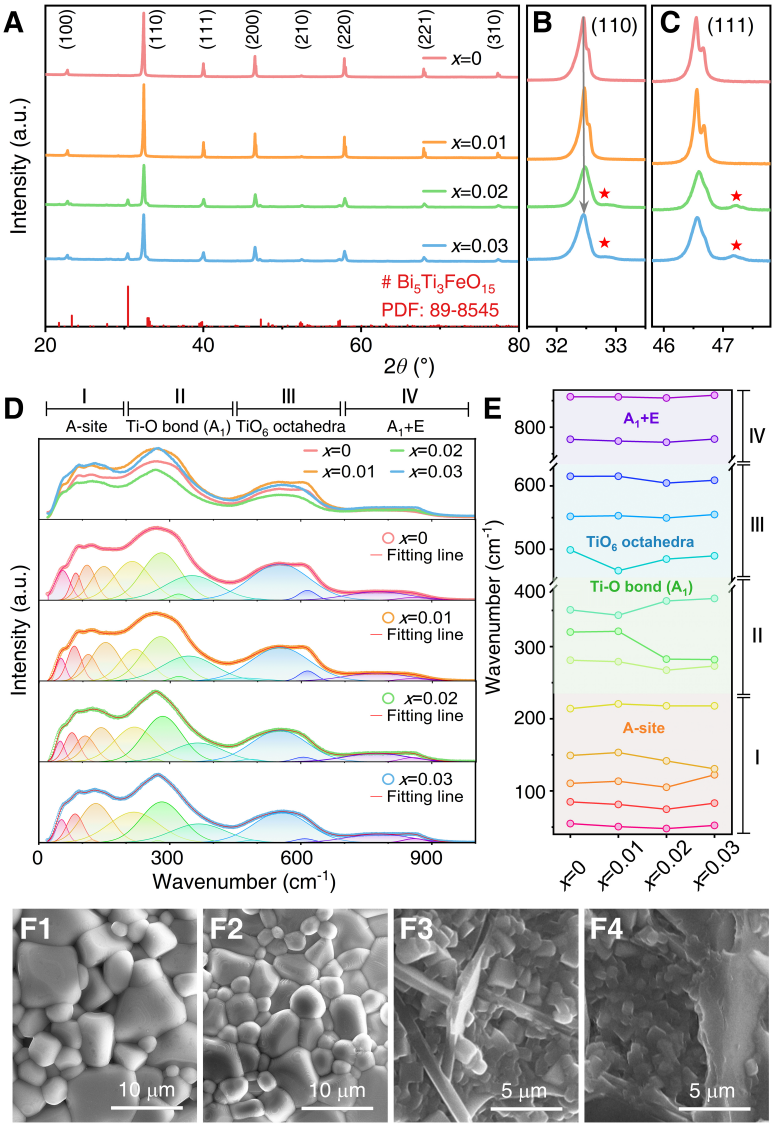

Figure 1. Microstructure and surface morphology of BNST-*x*FN ceramic samples after thermal etching. (A) X-ray diffraction (XRD) patterns of BNST-*x*FN ceramics, with red pentagrams indicating the peaks corresponding to the impurity phase. (B) Enlarged view of the (111) diffraction peak. (C) Magnified image of the (200) diffraction peak. (D) Raman spectra of BNST-*x*FN ceramic samples, along with the results of fitting thirteen Gaussian-Lorentzian peaks. (E) Variation of the Gaussian-Lorentzian peak positions across the thirteen peaks. (F1-F4) Surface morphology maps of BNST-*x*FN ceramics after thermal etching: (F1) $x = 0$, (F2) $x = 0.01$, (F3) $x = 0.02$, and (F4) $x = 0.03$.

peak profiles. However, in regions II and III, the peaks of BNST-0.01FN are noticeably broader than those of BNST. This broadening is attributed to the doping of $(Fe_{0.5}Nb_{0.5})^{4+}$ ions, which increases ion disorder and facilitates the transition to the ER phase[40]. In contrast, BNST-0.02FN and BNST-0.03FN show distinctly different spectra, likely due to the formation of the impurity phase and Enhanced relaxation. The presence of impurity phases notably affects both the microstructure and morphology of the ceramics. As shown in Figure 1F1-F4, the surface morphology of the ceramics is visibly altered after thermal etching. Doping with 1 mol.% $(Fe_{0.5}Nb_{0.5})^{4+}$ does not significantly affect the grain morphology but reduces the grain size. However, with further increases in doping, distinct lamellar impurity phase grains emerge in the ceramics, and their number increases with the doping content, inhibiting the growth of the normal perovskite grains.

The structure and grain evolution of ceramics directly influence their electrical properties. Figure 2 presents the dielectric and ferroelectric characteristics of the BNST-*x*FN ceramic samples. Specifically, Figure 2A-D shows the temperature-dependent variations of the dielectric constant (ε_r) and dielectric loss (tanδ) of the poled BNST-*x*FN ceramics, measured from RT to 450 °C at different frequencies. Prior to reaching the maximum dielectric constant (ε_m), ε_r exhibits frequency dispersion as a function of frequency. This behavior is attributed to the relaxation characteristics of the polarization response within the dielectric material. At a constant temperature, an increase in frequency typically results in a slight decrease in ε_r. This trend is due to the fact that at lower frequencies, the polarization mechanisms within the material have sufficient time to fully flourish, thereby enhancing the dielectric response. This phenomenon is not unique to BNT-based materials; it is a common feature observed in many relaxor ferroelectrics[49,50]. For the BNST and BNST-0.01FN samples, the ε_r begins to decline above the characteristic temperature (T_m), which corresponds to the ε_m. This decrease is attributed to the weakening of the polarization response associated with the paraelectric phase. Concurrently, the frequency dispersion is significantly reduced, indicating that the relaxation processes are suppressed at elevated temperatures[51].

In contrast, BNST-0.02FN and BNST-0.03FN display significant frequency dispersion throughout the entire temperature range[21]. This behavior is likely associated with the complex nature of the polarization mechanisms in these materials. Specifically, the presence of polar nanoregions (PNRs) and the formation of impurity phase, as illustrated in Figure 1F3 and F4, significantly influence the dielectric response. These structural features introduce local inhomogeneities that enhance the relaxor behavior, leading to the observed frequency dispersion[52]. Notably, a sharp increase in both ε_r and tanδ, especially at low frequencies (1 kHz), is observed at temperatures exceeding 300 °C. This phenomenon is commonly observed in ferroelectric ceramics based on BNT and BT and is attributed to the activation of conductive mechanisms, which are likely related to enhanced ionic conductivity and/or the presence of oxygen vacancies at elevated temperatures[21].

The introduction of the paraelectric phase, ST, leads to a marked decrease in the Curie temperature (T_C) of the ceramics, compared to the 320 °C typically observed for BNT[53]. However, doping with $(Fe_{0.5}Nb_{0.5})^{4+}$ has a minimal effect on T_m, with only slight fluctuations in the temperatures across all four samples. This indicates that the $(Fe_{0.5}Nb_{0.5})^{4+}$ dopants primarily influence the relaxation behavior rather than the ferroelectric phase transition temperature. In addition to the primary dielectric anomaly peak corresponding to the ε_m, a second anomaly peak appears in BNST, more prominently visible in the tanδ curve (inset of Figure 2A). This anomaly is characteristic of the poled NER-phase BNT-based ceramics and marks the transition from the ferroelectric phase to the relaxor phase, which is defined as the T_{FR}. Upon doping with $(Fe_{0.5}Nb_{0.5})^{4+}$, the T_{FR} for the other three samples shifts below RT, indicating that the ceramic samples transition from the NER phase to the ER phase.

To visualize the impact of $(Fe_{0.5}Nb_{0.5})^{4+}$ doping on the dielectric properties of the ceramics, we have analyzed the temperature-dependent variation of the ε_r at a frequency of 1 MHz, as shown in Figure 2E. The characteristic temperatures and ε_m extracted from these dielectric properties are summarized in Figure 2F. The results indicate that the ε_r curves flatten as the doping level of $(Fe_{0.5}Nb_{0.5})^{4+}$ increases, suggesting that $(Fe_{0.5}Nb_{0.5})^{4+}$ doping significantly enhances the dielectric relaxation in the ceramics. Specifically, the ε_m value remains relatively stable for BNST-0.01FN but decreases significantly with further doping (in BNST-0.02FN and BNST-0.03FN). This behavior is attributed to two primary factors. First, higher concentrations of $(Fe_{0.5}Nb_{0.5})^{4+}$ ions enhance dielectric relaxation. Second, the formation of impurity phases at elevated doping levels disrupts long-range ferroelectric ordering and introduces localized structural inhomogeneities. Collectively, these factors degrade the overall dielectric properties of the ceramics[21,52].

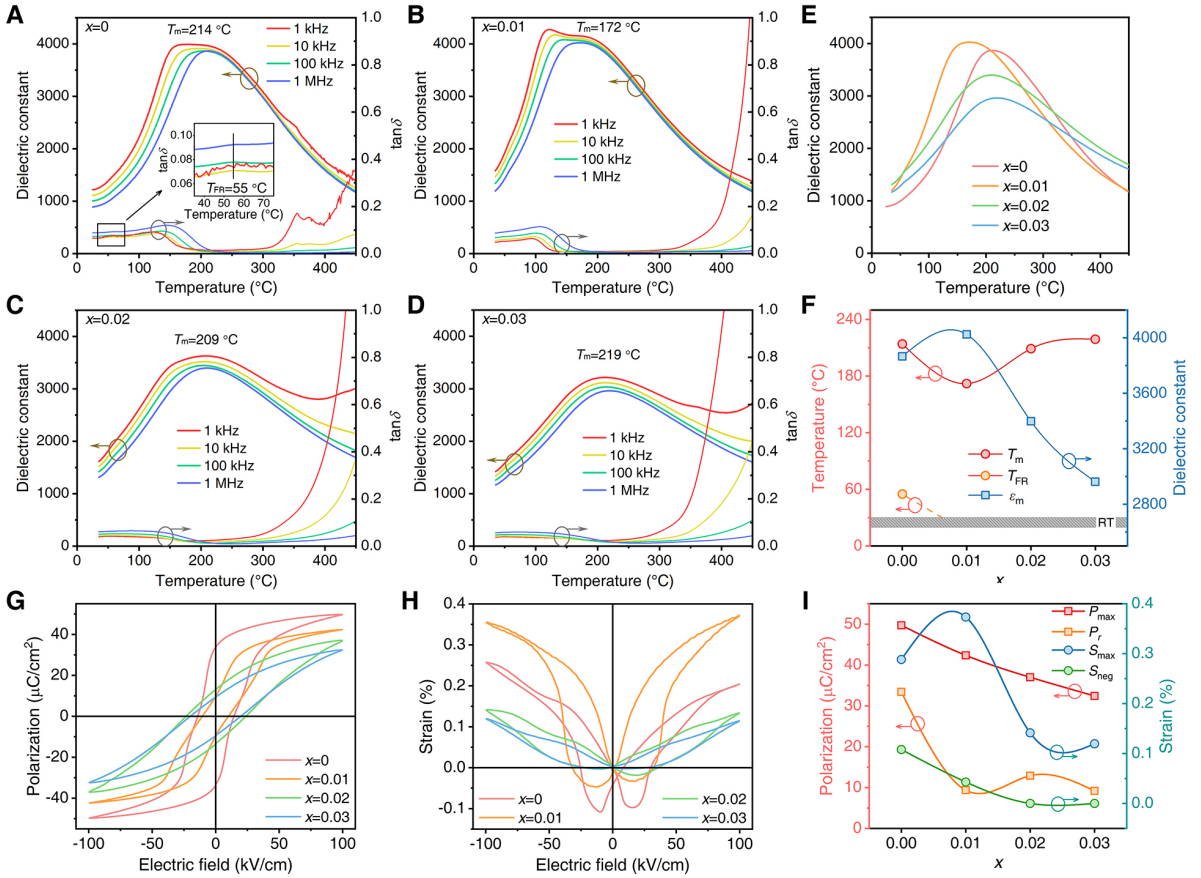

Figure 2. Dielectric and ferroelectric properties of BNST-*x*FN ceramic samples. (A-D) Dielectric constant (ε_r) and dielectric loss (tanδ) of BNST-xFN ceramics measured at 1, 10, and 100 kHz, 1 MHz as a function of temperature from room temperature (RT) to 450 °C (A: x = 0; B: x = 0.01; C: x = 0.02; D: x = 0.03). (E) Comparison of curves of ε_r at 1 MHz for BNST-*x*FN ceramic samples. (F) T_m, T_{FR} and ε_{max} as a function of x. (G) *P-E* loops of BNST-*x*FN ceramic samples at 100 kV/cm and 3 Hz. (H) *S-E* curves of BNST-*x*FN ceramic samples at 100 kV/cm and 3 Hz. (I) Variations in P_{max}, P_r, S_{max} and S_{neg} as a function of x.

The ferroelectric properties also exhibit significant changes with increasing doping. As shown in Figure 2G, BNST displays a typical ferroelectric hysteresis loop at 100 kV/cm, while the *P-E* loop of BNST-0.01FN shows a pronounced pinched shape. With further doping, the *P-E* loop becomes increasingly inclined, and the maximum polarization (P_{max}) decreases substantially. However, the remnant polarization (P_r) exhibits an upward trend, likely due to the formation of impurity phases. As observed in the *S-E* curves in Figure 2H, the butterfly-shaped curve of BNST transforms into a sprout-shaped curve following the doping of 1 mol.% $(Fe_{0.5}Nb_{0.5})^{4+}$. Correspondingly, the maximum electrostrain (S_{max}) increases significantly, and the negative electrostrain (S_{neg}) almost vanishes, indicating that the recoverable electrostrain results from the reversible nonpolar-to-polar phase transition of the ER-phase ceramic under the applied electric field. With further doping, the enhanced relaxation and the presence of non-ferroelectric second phases lead to a marked decrease in S_{max}. The ferroelectric parameters are summarized in Figure 2I.

The significant differences in dielectric and ferroelectric properties suggest that ceramic samples with distinct phase structures exhibit fundamentally different responses to electric field stimuli. As shown in Figure 3A, the *J-E* curves of BNST under an applied electric field exhibit four centrosymmetric peaks, with all positive current density peaks located in the first quadrant. Peak P_1 corresponds to domain switching in a typical ferroelectric, while peak P_2, appearing at higher electric fields, is associated with the presence of PNRs, which exhibit relatively weak current peaks[54].

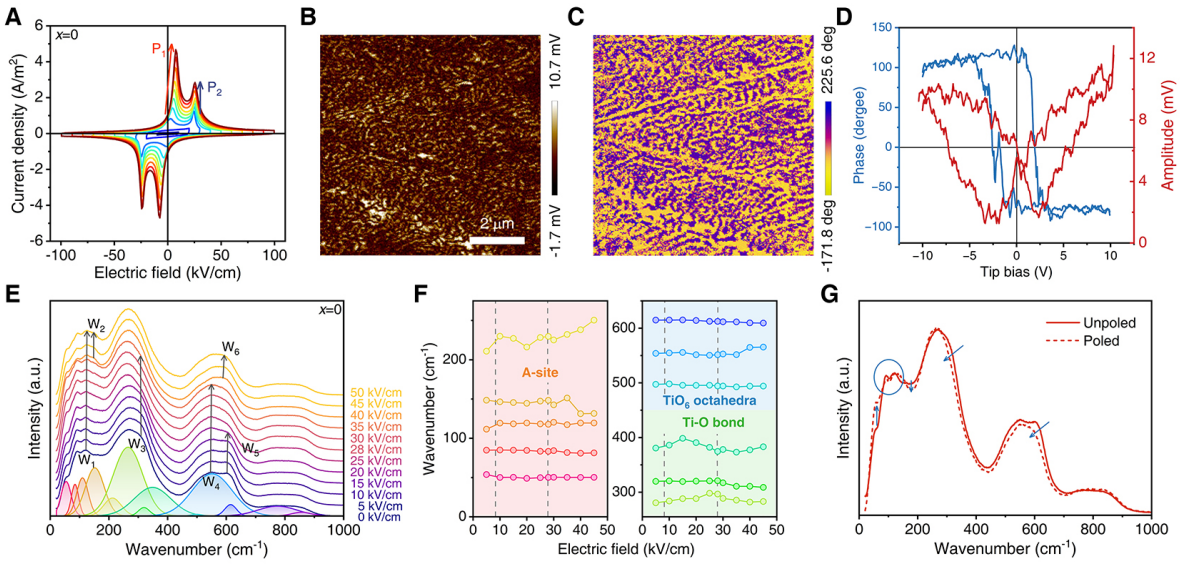

Figure 3. Polarization response and microstructure under electric field of BNST ceramic. (A) *J-E* curves of BNST ceramic samples at different applied electric fields. (B) Amplitude image and (C) phase image of domain structures in BNST ceramic. (D) Local switching spectra obtained via PFM, showing phase and amplitude response as a function of electric field. (E) Raman spectra and the fitting results of thirteen Gaussian-Lorentzian peaks for BNST ceramic at varying electric fields. (F) Variation of Gaussian-Lorentzian peak positions in regions I-III as a function of electric field. (G) Comparison of Raman spectra for poled and unpoled BNST samples.

The simultaneous presence of these two peaks indicates that the response to the electric field in BNST is primarily driven by domain switching, superimposed by the effects of PNRs. To further investigate the polarization response of the BNST sample, we performed PFM tests, and the results are shown in Figure 3B-D. Figure 3B presents the amplitude image of the polished ceramic surface, and Figure 3C displays the corresponding phase image. These images clearly reveal that the BNST ceramic exhibits a uniform and finely structured nano-scale domain arrangement. Additionally, the amplitude and phase curves, obtained by applying a periodic bias to the surface domains, are shown in Figure 3D. The consistency between these curves and the shapes of the *P-E* loop and *S-E* curve of BNST provides compelling microscopic evidence for the polarization behavior of BNST ceramics.

In-situ analysis techniques offer an intuitive means to explore the evolution of materials under the influence of electric fields[40]. As shown in Figure 3E and F, we present the results of *in-situ* Raman spectra under applied electric fields. Figure 3E reveals significant changes in the vibrational modes of the A-site, B-O bond, and BO_6 octahedron as the electric field is progressively enhanced. In Region I, the peak corresponding to W_1 evolves from being flush with the left peak to significantly surpassing it, while peak W_2 gradually emerges as the electric field reaches 40 kV/cm. These observations indicate a distinct phase transition in the ceramic samples under the electric field, leading to changes at the atomic and bond scales. In Region II, the peak corresponding to the B-O bond sharpens and becomes more concentrated, suggesting that the applied electric field induces a transition from disorder to order within the lattice[40,44], a phenomenon also observed in other BNT-based materials, implying enhanced polarity of the unit cell[40,44]. The most prominent change occurs in the vibrational modes of the BO_6 octahedron, where the W_4 peak persists up to 35 kV/cm, while the W_5 peak, present in the absence of the electric field, gradually diminishes as the field increases. This shift causes the BO_6 octahedron vibrational mode to transition from broadening to concentration, mirroring the trend in Region II, and indicates that the nanodomains generated by bond weakening are aligned under the applied electric field, promoting polarity through a transition from

disorder to order[40,44]. Notably, the electric field intensities corresponding to the P_1 and P_2 peaks in the *J-E* curve depicted in Figure 3A are 7.3 and 25.4 kV/cm, respectively. These peaks are indicative of distinct modes in the polarization response of the ceramics under an applied electric field. The P_1 peak, occurring at a lower electric field, is associated with domain switching, while the P_2 peak at higher electric fields is dominated by the arrangement of PNRs. As the applied electric field increases in Figure 3E, the W_5 peak existing in the initial state disappears between 20 and 25 kV/cm. This disappearance coincides precisely with the electric field range between the P_1 and P_2 peaks in the *J-E* curve [Figure 3A]. This observation suggests that domain switching is complete and an ordered evolution of the polarization response has occurred.

As the electric field reaches 40 kV/cm, peak W_4 is replaced by W_6, indicating a significant change in the polarization response. At this stage, the domain flip has already been completed, and the response from the PNRs becomes more diffuse and less pronounced above the P_1 peak. This indicates that these regions are contributing to the overall polarization but are not as sharply defined as the primary domain-switching peaks. This behavior is consistent with the relaxor nature of BNST ceramics, where the presence of PNRs leads to a broad and diffuse polarization response rather than sharp transitions[21].

The peak position change curves for different peaks in each region, as shown in Figure 3F, further confirm that the inflection points of the peak shifts in the *in-situ* Raman spectra often correspond to the polarization response modes of BNST under different electric field strengths, as observed in Figure 3A. This correspondence underscores the close relationship between microstructural changes and the polarization response in BNST ceramic. The initial sharp peaks (W_4 and W_5) are associated with domain switching, while the later peaks (W_6) and the diffuse response from the PNRs indicate a more complex interplay between domain alignment and PNR reorientation. This finding highlights the importance of understanding the microstructural changes that occur under an applied electric field, as these changes significantly influence the macroscopic electrical properties of the material[55]. Finally, a comparison of the Raman spectra of poled and unpoled ceramics in Figure 3G provides a more intuitive understanding of the narrowing of B-O bonding and BO_6 octahedron vibrational peaks, along with changes in peak shapes and intensities in Region I[51]. These results clearly demonstrate that the electric field induces a phase structure change in the ceramic samples, which in turn influences the arrangement of A-site ions in the lattice.

For BNST-0.01FN, Figure 4A shows that the peak P_1 has significantly reduced in intensity and shifted to the second quadrant, compared to BNST. This suggests that the ceramic material tends to revert to a nonpolar state upon removal of the electric field. However, the persistence of a significant intensity for peak P_1, along with its broadening, continues until the electric field is reduced to zero, indicating that some domain switching remains within the ceramic. This observation is further supported by the PFM results presented in Figure 4B-D. The amplitude and phase images in Figure 4B and C reveal that BNST-0.01FN consists of nanodomains with noticeably reduced sizes, as well as regions that exhibit no domain response, likely corresponding to the PNRs. Additionally, the amplitude image in Figure 4D aligns with the *S-E* curve of BNST-0.01FN, showing no negative electrostrain, which further corroborates the absence of a negative electrostrain response in the material.

In comparison with the Raman spectra of BNST under an *in-situ* electric field, the results for BNST-0.01FN, presented in Figure 4E-G, show notable differences. The Raman spectra under varying applied electric fields, as shown in Figure 4E, reveal that the A-site vibrational modes remain largely unaffected, while the peaks corresponding to the B-O bond and BO_6 octahedra undergo significant evolution. This suggests that the applied electric field induces a transition from disorder to order within the lattice, enhancing the polarity of the unit cell[40,44]. As indicated by the peak shifts in Figure 4F, the primary fluctuation occurs in

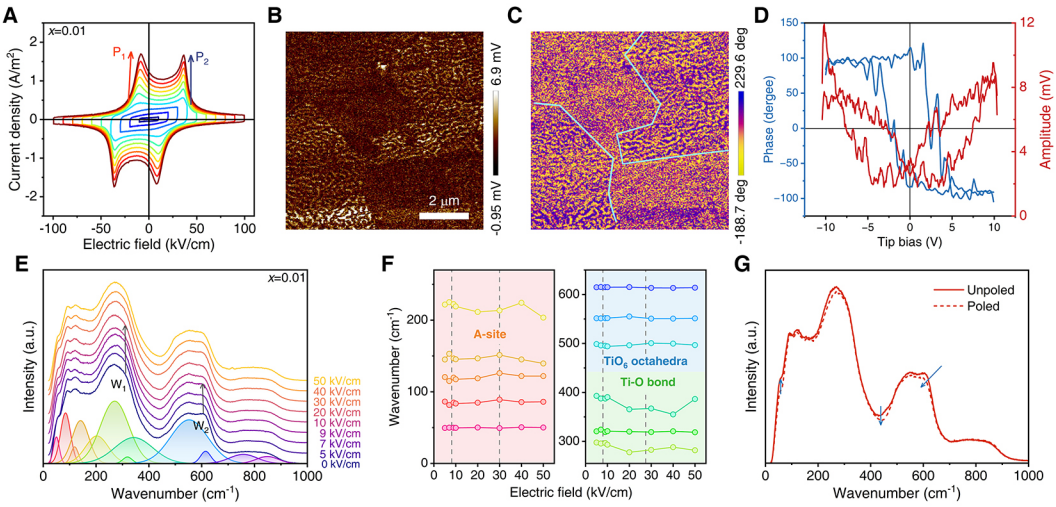

Figure 4. Polarization response and microstructure under electric field of BNST-0.01FN ceramic. (A) *J-E* curves of BNST-0.01FN ceramic samples at different applied electric fields. (B) Amplitude image and (C) phase image of domain structures in BNST-0.01FN ceramic. (D) Local switching spectra obtained via PFM, showing phase and amplitude response as a function of electric field. (E) Raman spectra and the fitting results of thirteen Gaussian-Lorentzian peaks for BNST-0.01FN ceramic at various electric fields. (F) Variation of Gaussian-Lorentzian peak positions in regions I-III as a function of electric field. (G) Comparison of Raman spectra for poled and unpoled BNST-0.01FN samples.

region II, which corresponds to the B-O bond vibrational mode, with the A-site ions near the B-O bond (around 200 cm^{-1}) being the most affected by this fluctuation. This change is most pronounced in the comparative curves shown in Figure 4G. The doping of $(Fe_{0.5}Nb_{0.5})^{4+}$ leads to a more pronounced response from the PNRs within the ceramic, which align under the applied electric field. However, this response has little impact on the lattice structure itself, resulting in the narrowing of the vibrational mode peaks for the B-O bond and BO_6 octahedra, while the A-site vibrational modes remain almost unchanged.

As doping increases to BNST-0.03FN, no distinct current density peaks are observed in the *J-E* curves, as shown in Figure 5A, and the domain structure becomes increasingly undefined, as seen in Figure 5B and C. In BNST-0.03FN, only the tiny PNR response contributes to polarization, resulting in weak signal feedback in the phase and amplitude images at high applied bias, as shown in Figure 5D. This behavior corresponds to a significant reduction in both P_{max} and S_{max} in the *P-E* loop and *S-E* curve. The *in-situ* Raman spectra, presented in Figure 5E and F, also show minimal changes, with only slight fluctuations in peak positions at high electric fields. Notably, the Raman spectra of the poled and unpoled samples almost entirely overlap, as shown in Figure 5G, indicating that the vibrational modes and lattice structures remain stable. These results suggest that as $(Fe_{0.5}Nb_{0.5})^{4+}$ doping increases, the ferroelectric characteristics of the ceramic gradually diminish, and its response to the applied electric field becomes increasingly less sensitive.

The analysis of Figures 2-5 reveals that ion doping can effectively modify the characteristic temperature of BNT-based ceramics and influence their phase structure, leading to optimized and enhanced material properties. Further investigation into the evolution of phase structures in BNT-based materials with varying doping levels, along with the corresponding microscopic polarization response and macroscopic property changes, is an important avenue for future research. To this end, we conducted detailed studies on the structural, polarization, and ferroelectric property variations of three different ceramic samples during the heating process. The results of these studies are presented in Figures 6-8.

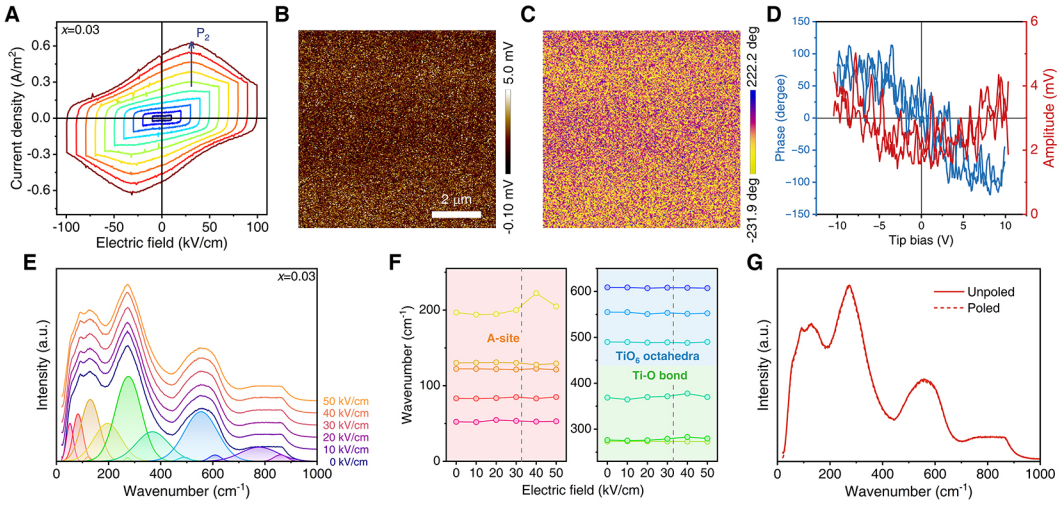

Figure 5. Polarization response and microstructure under electric field of BNST-0.03FN ceramic. (A) *J-E* curves of BNST-0.03FN ceramic samples at different applied electric fields. (B) Amplitude image and (C) phase image of domain structures in BNST-0.03FN ceramic. (D) Local switching spectra obtained via PFM, showing phase and amplitude response as a function of electric field. (E) Raman spectra and the fitting results of thirteen Gaussian-Lorentzian peaks for BNST-0.03FN ceramic at various electric fields. (F) Variation of Gaussian-Lorentzian peak positions in regions I-III as a function of electric field. (G) Comparison of Raman spectra for poled and unpoled BNST-0.03FN samples.

The evolution of the *P-E* loops and *S-E* curves with increasing temperature for BNST, along with the corresponding ferroelectric parameters, is shown in Figure 6A-C. As the temperature increases, the *P-E* loops of BNST gradually exhibit a pinched shape, accompanied by a significant decrease in P_{max} at a certain temperature. Notably, the S_{neg} gradually disappears, while the S_{max} increases, reaching a peak of 0.38% near the T_{FR}. Interestingly, as the temperature rises, the *P-E* loops and *S-E* curves of BNST evolve toward the features observed in BNST-0.01FN. To gain deeper insight into the polarization response, *J-E* curves were measured at various temperatures, and the two-dimensional evolution of the first and second quadrant *J-E* curves with temperature is depicted in Figure 6D and E. The results show that peak P_1 shifts toward lower electric fields as the temperature increases, eventually moving to the second quadrant, such as BNST-0.01FN. In contrast, peak P_2 moves in the opposite direction, and the intensities of both peaks gradually decrease, ultimately merging into a broad peak without distinct current maxima at high temperatures. This indicates a transition from the NER to the ER phase during heating, with the contribution of domain switching decreasing. Consequently, the *P-E* loop girdles, and S_{neg} decreases. As the ceramic reaches the boundary between the NER and ER phases, the potential barrier between these phases diminishes due to the proximity of the free energies of the electric field-induced ferroelectric and ER phases, leading to a significant enhancement of electrostrain performance[56]. Upon further heating, as BNST fully transitions to the ER phase, the size and number of PNRs decrease, weakening the polarization contribution. This results in a reduction of both P_{max} and S_{max} due to the increased potential barrier in the ER phase and a decrease in the free energy of the ER phase.

XRD and Raman spectroscopy were employed to investigate the structural evolution of the ceramics with temperature, as shown in Figure 6F-H. Figure 6F presents the evolution of the (111) and (200) peaks of the poled sample during the heating process. Notably, the shoulder of the (111) peak, highlighted by the orange circle at RT, evolves into a distinct peak as the temperature increases, completing this transition near the T_{FR}. This suggests that the polarization generated by domain switching in BNST at RT can only be sustained up to the T_{FR}. Above this temperature, the ceramic undergoes a transition from the NER phase to the ER phase. In the ER phase, the contribution of PNRs to polarization becomes recoverable upon the removal of

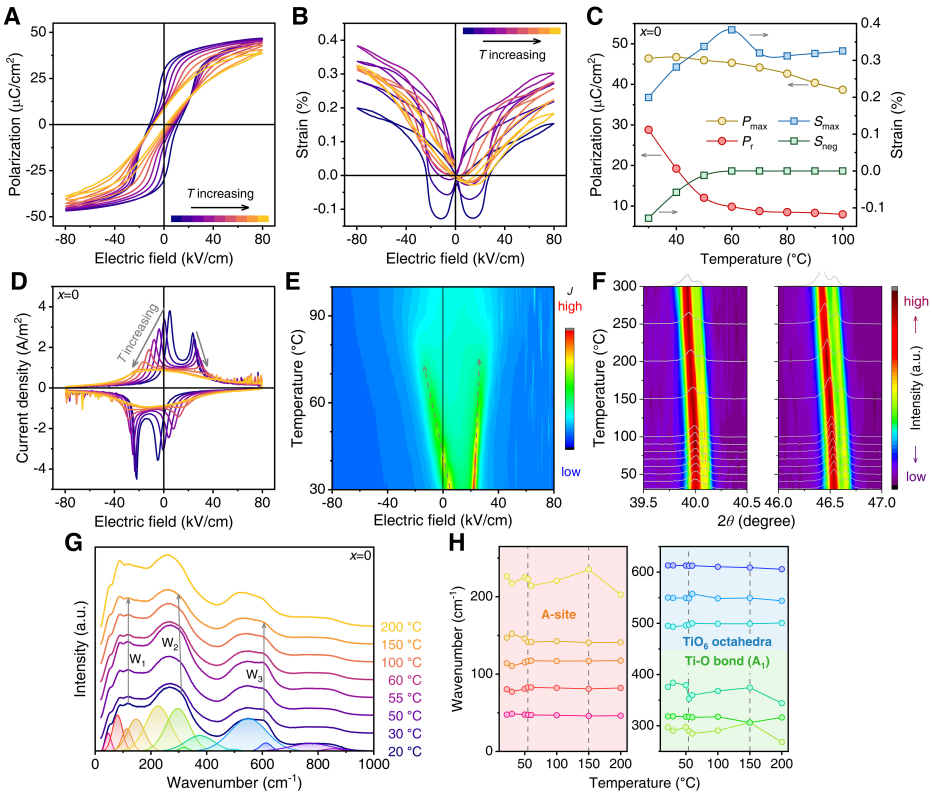

Figure 6. Ferroelectric properties, polarization response, and microstructure during the heating process of BNST ceramic. (A) *P-E* loops and (B) *S-E* curves of BNST ceramic at different temperatures. (C) Variation of P_{max}, P_r, S_{max} and S_{neg} as a function of temperature. (D) *J-E* curves of BNST ceramic at different temperatures. (E) Two-dimensional evolution of the *J-E* curves with temperature in the first and second quadrants. (F) XRD pattern showing the evolution of the (111) peak and (200) peak with temperature of BNST ceramic. (G) Raman spectra and the fitting results of thirteen Gaussian-Lorentzian peaks for BNST ceramic at different temperatures. (H) Variation of Gaussian-Lorentzian peak positions in regions I-III as a function of temperature.

the electric field, reflecting the key difference between the phase transitions of the NER and ER phases under electric field application, with the former being irreversible and the latter reversible. Beyond the T_{FR}, the phase structure remains stable, and only lattice expansion due to the high temperature is observed, causing both the (111) and (200) peaks to shift to lower angles. Similarly, the Raman spectra in Figure 6G and H show distinct changes with increasing temperature. The lattice expansion induced by temperature leads to noticeable alterations in the vibrational modes of the A-site ions, with peak W_1 gradually weakening while the peak on the left intensifies. Peaks at W_2 and W_3 remain prominent until near the T_{FR}, after which they begin to weaken. These temperature-induced changes are most clear in Figure 6H, where all the peaks exhibit marked changes at the T_{FR}, further confirming that a phase transition occurs at this point.

For BNST-0.01FN, which is already in the ER phase, the *P-E* loops shown in Figure 7A gradually evolve from a pinched to an inclined shape with increasing temperature. This behavior is consistent with the *S-E* curves in Figure 7B, where both P_{max} and S_{max} decrease progressively. As shown in Figure 7C, the temperature dependence of P_{max}, S_{max}, and P_r indicates a gradual reduction in all parameters without any abrupt transitions, suggesting that ceramics in the ER phase exhibit enhanced relaxation behavior under elevated temperatures. This observation is further confirmed in Figure 7D and E, where the two current density peaks significantly diminish in intensity and eventually disappear with increasing temperature. The *J-E* curve forms a broad bulge, signaling a decrease in the size and number of PNRs, and a weakening of the

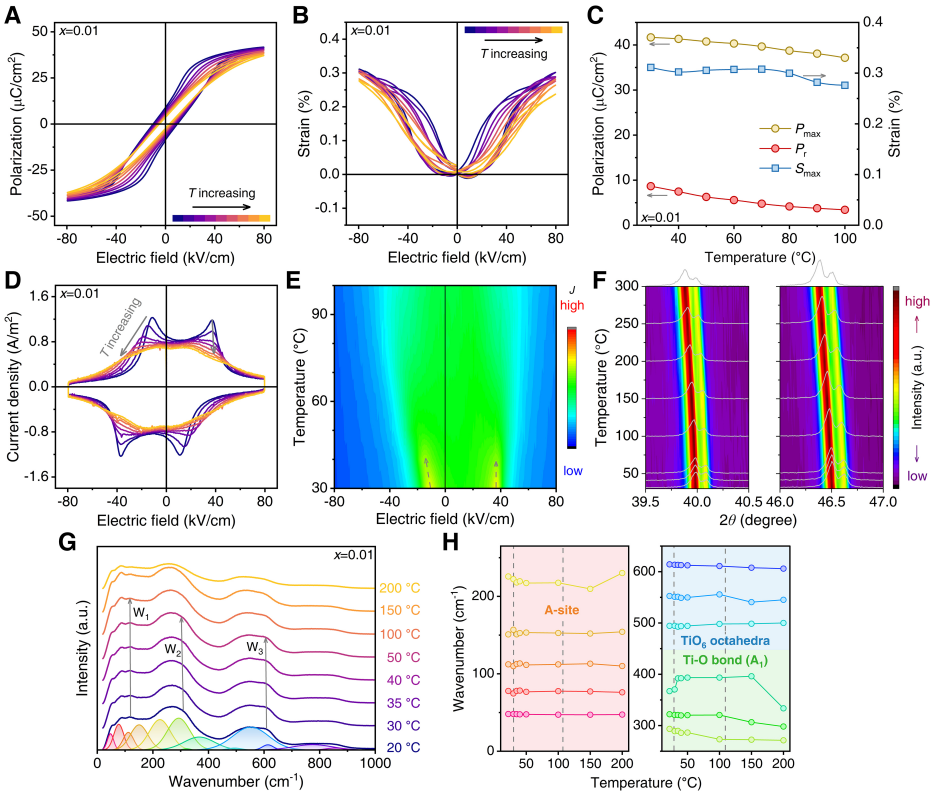

Figure 7. Ferroelectric properties, polarization response, and microstructure during the heating process of BNST-0.01FN ceramic. (A) *P-E* loops and (B) *S-E* curves of BNST-0.01FN ceramic at different temperatures. (C) Variation of P_{max}, P_r, S_{max} and S_{neg} as a function of temperature. (D) *J-E* curves of BNST-0.01FN ceramic at different temperatures. (E) Two-dimensional evolution of the *J-E* curves with temperature in the first and second quadrants. (F) XRD pattern showing the evolution of the (111) peak and (200) peak with temperature of BNST-0.01FN ceramic. (G) Raman spectra and the fitting results of thirteen Gaussian-Lorentzian peaks for BNST-0.01FN ceramic at different temperatures. (H) Variation of Gaussian-Lorentzian peak positions in regions I-III as a function of temperature.

polarization contribution. As a result, the ability of the ceramic to induce a strong polar state under an applied electric field is diminished.

XRD results in Figure 7F show no changes in phase structure, with the (111) and (200) peaks merely shifting to lower angles due to temperature-induced lattice expansion. Similarly, the Raman spectra in Figure 7G and H display only minor shifts in peak positions, consistent with lattice stretching at high temperatures, with no evidence of a phase transition. Taken together, these results confirm the structural and property evolution of BNST-0.01FN at elevated temperatures, reinforcing the transition towards a more relaxed state as temperature increases.

A similar phenomenon was observed in the BNST-0.03FN ceramic sample, with even more stable *P-E* loops and *S-E* curves, as well as corresponding P_{max}, S_{max} and P_r parameters shown in Figure 8A-C. However, the *J-E* curves in Figure 8D exhibit a slight change, with the bulge in the first quadrant flattening as the temperature increases. This behavior suggests that the size and number of PNRs in BNST-0.03FN also decrease with temperature, leading to a relatively weaker polarization response. Figure 8E further confirms this trend, as the current density significantly diminishes. In the temperature-dependent XRD and Raman spectra results shown in Figure 8F-H, only changes due to lattice expansion are observed, indicating that the material's structural integrity remains stable at elevated temperatures. These findings suggest that BNST-

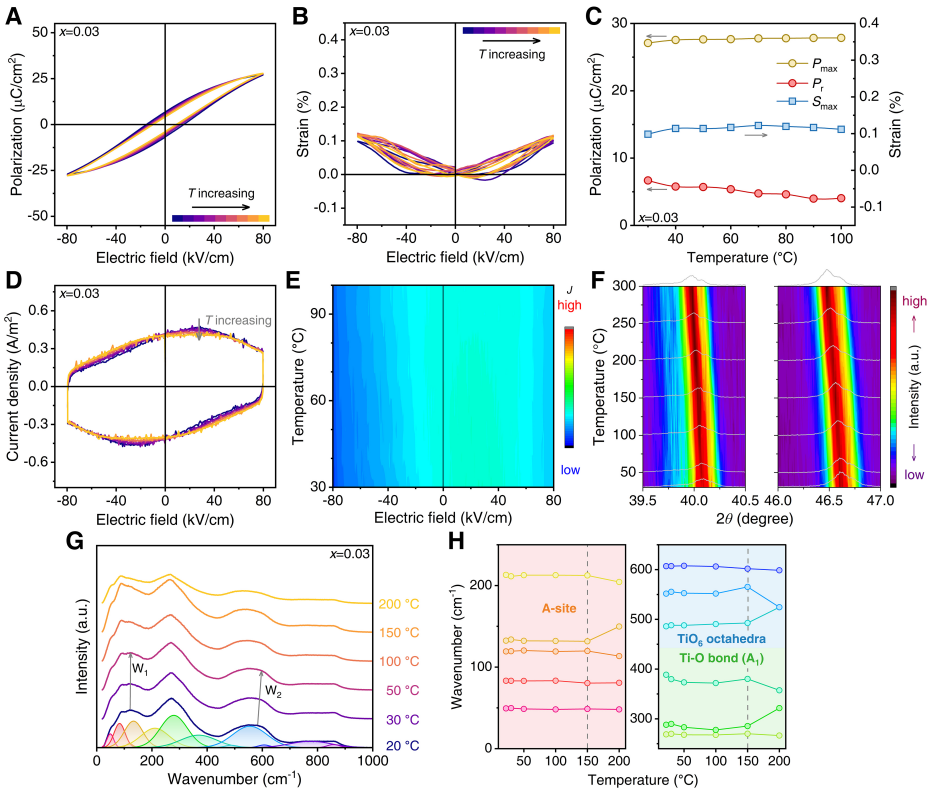

Figure 8. Ferroelectric properties, polarization response, and microstructure during the heating process of BNST-0.03FN ceramic. (A) *P-E* loops and (B) *S-E* curves of BNST-0.03FN ceramic at different temperatures. (C) Variation of P_{max}, P_r, S_{max} and S_{neg} as a function of temperature. (D) *J-E* curves of BNST-0.03FN ceramic at different temperatures. (E) Two-dimensional evolution of the *J-E* curves with temperature in the first and second quadrants. (F) XRD pattern showing the evolution of the (111) peak and (200) peak with temperature of BNST-0.03FN ceramic. (G) Raman spectra and the fitting results of thirteen Gaussian-Lorentzian peaks for BNST-0.03FN ceramic at different temperatures. (H) Variation of Gaussian-Lorentzian peak positions in regions I-III as a function of temperature.

0.03FN undergoes a decrease in PNR response to the electric field and a weakening of polarization properties at high temperatures. However, the structure primarily exhibits lattice expansion without undergoing a significant phase transition.

The above analyses reveal that the phase structure of ceramics can be modulated through doping and temperature control, which in turn affects their response behavior and ferroelectric properties under an applied electric field. To better illustrate these findings, we constructed the schematic shown in Figure 9. Figure 9A illustrates that BNST ceramics below the T_{FR} are in the NER phase. As indicated by the clear relaxation behavior observed in the dielectric constant profile [Figure 2A] and the distinct distribution of domains revealed by PFM results [Figure 3C], the initial microstructure of BNST consists of isotropic domains interspersed with a small number of PNRs, as depicted in Figure 9B. When an electric field is applied, both domain switching and the alignment of the PNRs contribute to the polarization response. This dual mechanism results in four centrosymmetric current density peaks in the first and fourth quadrants of the *J-E* curve, as shown in Figure 9C. At low electric fields, the current density peaks primarily arise from domain switching, which is accompanied by a sharp increase in polarization in the *P-E* loop and the appearance of S_{neg} in the *S-E* curve. This behavior is indicative of the significant contribution of domain reorientation to the polarization response, as commonly observed in ferroelectric materials. Conversely, the current peaks at higher electric fields are associated with the alignment of the PNRs. At this point, the

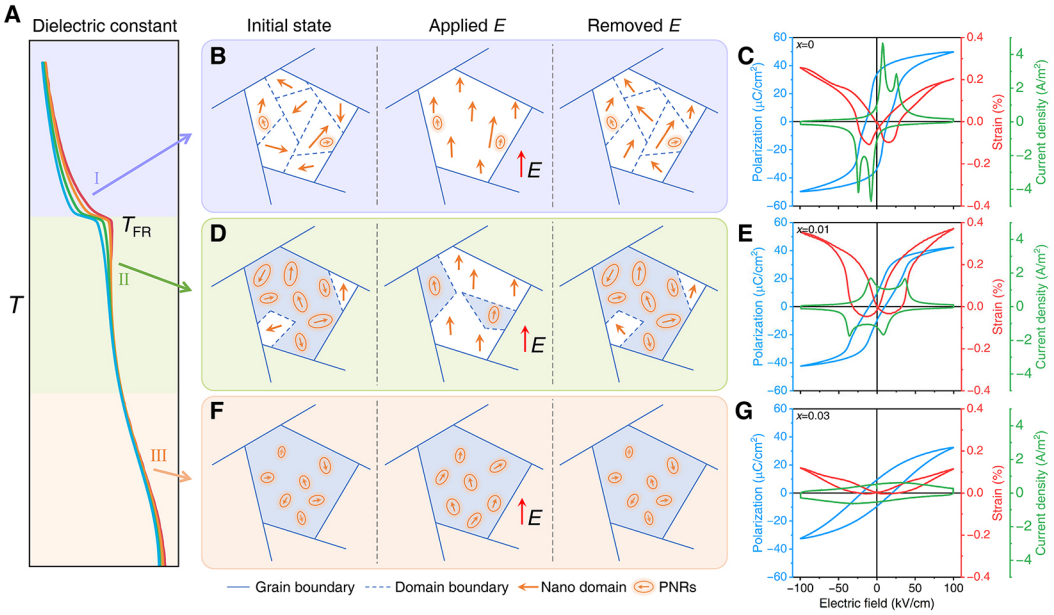

Figure 9. Polarization response and macroscopic properties of ceramics with different phase structures. (A) Schematic showing the dielectric constant as a function of temperature for BNST-*x*FN ceramics, with BNST, BNST-0.01FN, and BNST-0.03FN represented at distinct positions along the curve. (B) Initial domain structure, polarization response under an applied electric field, and after field removal for BNST ceramic. (C) *P-E* loops, *S-E* curve and *J-E* curve of BNST ceramic. (D) Initial domain structure, polarization response under an applied electric field, and after field removal for BNST-0.01FN ceramic. (E) *P-E* loops, *S-E* curve and *J-E* curve of BNST-0.01FN ceramic. (F) Initial domain structure, polarization response under an applied electric field, and after field removal for BNST-0.03FN ceramic. (G) *P-E* loops, *S-E* curve and *J-E* curve of BNST-0.03FN ceramic.

increase in polarization in the *P-E* loop begins to slow down, suggesting that the PNRs are gradually contributing to the overall polarization response. Importantly, the transition from the NER phase to the ferroelectric phase is irreversible. Consequently, the microstructure cannot be restored to its original state upon removal of the electric field, as illustrated in Figure 9B. This irreversibility leads to a significant P_r in the *P-E* loop.

When 1 mol.% of $(Fe_{0.5}Nb_{0.5})^{4+}$ is doped into the ceramics, the dielectric profile shifts above the T_{FR}, as shown in Figure 9A. According to the PFM results in Figure 4B and C, BNST-0.01FN is situated at the phase boundary between the NER and ER phases. Its microstructure is dominated by PNRs, with a small number of significantly reduced-size nanodomains [Figure 9D]. Since the free energy at the phase boundary between the NER and ER phases is close to that of the ferroelectric phase, with a low potential barrier, the applied electric field can more easily induce a transition to the ferroelectric phase. This transition is reversible. Upon removal of the electric field, the PNR regions can recover, leading to the pinched *P-E* loop shown in Figure 9E (with a sharp decrease in P_r compared to BNST) and the near disappearance of S_{neg} in the *S-E* curve. Reversible nonpolar-to-polar phase transitions usually result in a significantly higher S_{max}.

With further doping, the dielectric curve shifts further away from the T_{FR}, and the relaxation of BNST-0.03FN is enhanced. In this case, the polarization response is primarily contributed by the smaller-sized PNRs, as shown in Figure 9F. Since the free energy is now significantly deviated from that of the ferroelectric phase, the electric field can no longer induce long-range ordered polarization, leading to a significant reduction in polarization, electrostrain, and current density responses, as shown in Figure 9G.

By comprehensively analyzing the structure, polarization response, and property effects of different phase structures of BNT-based ceramics under *in situ* electric field stimulation, combined with the temperature variation effects, we gain a deeper understanding of the evolution under the influence of chemical modification, electric field, and temperature. This understanding can help in the design of materials with enhanced electrostrain properties for lead-free actuator applications.

CONCLUSIONS

This study systematically investigates the phase structure evolution, polarization behavior, and electrical properties of BNST-*x*FN lead-free ferroelectric ceramics under the combined influences of electric field and temperature. Through a detailed analysis of the electrostrain behavior across ceramics with varying initial phase structures, we identify the mechanisms responsible for their distinct responses. Notably, BNST-0.01FN ceramics, located at the phase boundary between the NER and ER phases, undergo a reversible nonpolar-to-polar phase transition when subjected to an electric field, resulting in an electrostrain of 0.37%. Furthermore, BNST ceramics initially in the NER phase exhibit a gradual transition to the ER phase as the temperature increases, yielding a significant electrostrain of 0.38% under the synergistic effects of electric field and thermal stimuli. These findings underscore the dynamic interplay between microstructural evolution and macroscopic electrical properties, providing critical insights for the design of advanced lead-free actuator materials with enhanced electrostrain performance.

DECLARATIONS

Authors' contributions

Conceptualization, supervision, investigation, formal analysis, funding acquisition, writing - original draft: Jing, R.
Investigation, formal analysis: Man, W.
Data curation: Nie, X.
Formal analysis: Zhang, L.
Conceptualization, supervision, methodology, resources, project administration, funding acquisition, writing - review & editing: Jin, L.

Availability of data and materials

The rata data supporting the findings of this study are available within this Article and its Supplementary Material. Further data are available from the corresponding authors upon request.

Financial support and sponsorship

This work was finically supported by the National Natural Science Foundation of China (Grant Nos. 52302153 and 52261135548), the China Postdoctoral Science Foundation (Grant Nos. GZC20232075 and 2023M742767) and Shaanxi Province postdoctoral research project (Project No. 2023BSHTBZZ14). The SEM work was done at the International Center for Dielectric Research (ICDR), Xi'an Jiaotong University, Xi'an, China.

Conflicts of interest

All authors declared that there are no conflicts of interest.

Ethical approval and consent to participate

Not applicable.

Consent for publication

Not applicable.

REFERENCES

1. Jo, W.; Dittmer, R.; Acosta, M.; et al. Giant electric-field-induced strains in lead-free ceramics for actuator applications - status and perspective. *J. Electroceram.* **2012**, *29*, 71-93. DOI
2. Panda, P. K.; Sahoo, B. PZT to lead free piezo ceramics: a review. *Ferroelectrics* **2015**, *474*, 128-43. DOI
3. Yang, L.; Kong, X.; Li, F.; et al. Perovskite lead-free dielectrics for energy storage applications. *Prog. Mater. Sci.* **2019**, *102*, 72-108. DOI
4. Zhang, L.; Jing, R.; Huang, Y.; et al. Ultra-weak polarization-strain coupling effect boosts capacitive energy storage. *Adv. Mater.* **2024**, *36*, e2406219. DOI
5. Zhang, S. High entropy design: a new pathway to promote the piezoelectricity and dielectric energy storage in perovskite oxides. *Microstructures* **2023**, *3*, 2023003. DOI
6. Hao, J.; Li, W.; Zhai, J.; Chen, H. Progress in high-strain perovskite piezoelectric ceramics. *Mater. Sci. Eng. R. Rep.* **2019**, *135*, 1-57. DOI
7. Fan, P.; Liu, K.; Ma, W.; et al. Progress and perspective of high strain NBT-based lead-free piezoceramics and multilayer actuators. *J. Materiomics.* **2021**, *7*, 508-44. DOI
8. Wei, Y.; Deng, Y.; Dong, S.; et al. Enhancement of piezoelectric performance in $(Bi_{1/2}Na_{1/2})TiO_3$-based system through single-crystallization. *Chem. Eng. J.* **2024**, *496*, 153996. DOI
9. Li, F.; Wang, L.; Jin, L.; et al. Piezoelectric activity in Perovskite ferroelectric crystals. *IEEE. Trans. Ultrason. Ferroelectr. Freq. Control.* **2015**, *62*, 18-32. DOI
10. Zeng, J.; Zhao, K.; Shi, X.; Ruan, X.; Zheng, L.; Li, G. Large strain induced by the alignment of defect dipoles in (Bi^{3+},Fe^{3+}) co-doped $Pb(Zr,Ti)O_3$ ceramics. *Scripta. Mater.* **2018**, *142*, 20-2. DOI
11. Bian, L.; Qi, X.; Li, K.; et al. High-performance [001]c-textured PNN-PZT relaxor ferroelectric ceramics for electromechanical coupling devices. *Adv. Funct. Mater.* **2020**, *30*, 2001846. DOI
12. Panda, P. K. Review: environmental friendly lead-free piezoelectric materials. *J. Mater. Sci.* **2009**, *44*, 5049-62. DOI
13. Zheng, T.; Wu, J.; Xiao, D.; Zhu, J. Recent development in lead-free perovskite piezoelectric bulk materials. *Prog. Mater. Sci.* **2018**, *98*, 552-624. DOI
14. Wang, D.; Fan, Z.; Rao, G.; et al. Ultrahigh piezoelectricity in lead-free piezoceramics by synergistic design. *Nano. Energy.* **2020**, *76*, 104944. DOI
15. Zhang, S.; Kounga, A. B.; Aulbach, E.; Ehrenberg, H.; Rödel, J. Giant strain in lead-free piezoceramics $Bi_{0.5}Na_{0.5}TiO_3$-$BaTiO_3$-$K_{0.5}Na_{0.5}NbO_3$ system. *Appl. Phys. Lett.* **2007**, *91*, 112906. DOI
16. Viola, G.; Tian, Y.; Yu, C.; et al. Electric field-induced transformations in bismuth sodium titanate-based materials. *Prog. Mater. Sci.* **2021**, *122*, 100837. DOI
17. Zhou, X.; Xue, G.; Luo, H.; Bowen, C. R.; Zhang, D. Phase structure and properties of sodium bismuth titanate lead-free piezoelectric ceramics. *Prog. Mater. Sci.* **2021**, *122*, 100836. DOI
18. Wu, X.; Wu, C.; Yang, D.; Yin, J.; Wu, J. Strain regulation via composition and valence dependent substitution in BNT-based solid solutions. *Adv. Powder. Mater.* **2023**, *2*, 100079. DOI
19. Lai, L.; Li, B.; Tian, S.; Zhao, Z.; Zhang, S.; Dai, Y. Giant electrostrain in lead-free textured piezoceramics by defect dipole design. *Adv. Mater.* **2023**, *35*, e2300519. DOI
20. Li, T.; Liu, C.; Shi, P.; et al. High-performance strain of lead-free relaxor-ferroelectric piezoceramics by the morphotropic phase boundary modification. *Adv. Funct. Mater.* **2022**, *32*, 2202307. DOI
21. Jing, R.; Zhang, L.; Hu, Q.; et al. Phase evolution and relaxor to ferroelectric phase transition boosting ultrahigh electrostrains in $(1-x)(Bi_{1/2}Na_{1/2})TiO_3$-$x(Bi_{1/2}K_{1/2})TiO_3$ solid solutions. *J. Materiomics.* **2022**, *8*, 335-46. DOI
22. Wang, Z.; Zhao, J.; Zhang, N.; et al. Optimizing strain response in lead-free $(Bi_{0.5}Na_{0.5})TiO_3$-$BaTiO_3$-$NaNbO_3$ solid solutions via ferroelectric/(non-)ergodic relaxor phase boundary engineering. *J. Materiomics.* **2023**, *9*, 244-55. DOI
23. Malik, R. A.; Hussain, A.; Maqbool, A.; et al. Temperature-insensitive high strain in lead-free $Bi_{0.5}(Na_{0.84}K_{0.16})_{0.5}TiO_3$-$0.04SrTiO_3$ ceramics for actuator applications. *J. Am. Ceram. Soc.* **2015**, *98*, 3842-8. DOI
24. Zhang, X.; Jiang, G.; Liu, D.; Yang, B.; Cao, W. Enhanced electric field induced strain in $(1-x)((Bi_{0.5}Na_{0.5})TiO_3$-$Ba(Ti,Zr)O_3)$-$xSrTiO_3$ ceramics. *Ceram. Int.* **2018**, *44*, 12869-76. DOI
25. Bai, W.; Li, L.; Li, W.; Shen, B.; Zhai, J.; Chen, H. Effect of $SrTiO_3$ template on electric properties of textured BNT-BKT ceramics prepared by templated grain growth process. *J. Alloys. Compd.* **2014**, *603*, 149-57. DOI
26. Wang, F.; Xu, M.; Tang, Y.; et al. Large strain response in the ternary $Bi_{0.5}Na_{0.5}TiO_3$-$BaTiO_3$-$SrTiO_3$ solid solutions. *J. Am. Ceram. Soc.* **2012**, *95*, 1955-9. DOI

27. Lalitha, K. V.; Koruza, J.; Rödel, J. Propensity for spontaneous relaxor-ferroelectric transition in quenched $(Na_{1/2}Bi_{1/2})TiO_3$-$BaTiO_3$ compositions. *Appl. Phys. Lett.* **2018**, *113*, 252902. DOI
28. Li, T.; Lou, X.; Ke, X.; et al. Giant strain with low hysteresis in A-site-deficient $(Bi_{0.5}Na_{0.5})TiO_3$-based lead-free piezoceramics. *Acta. Mater.* **2017**, *128*, 337-44. DOI
29. Fan, P.; Zhang, Y.; Xie, B.; et al. Large electric-field-induced strain in B-site complex-ion $(Fe_{0.5}Nb_{0.5})^{4+}$-doped $Bi_{1/2}(Na_{0.82}K_{0.12})_{1/2}TiO_3$ lead-free piezoceramics. *Ceram. Int.* **2018**, *44*, 3211-7. DOI
30. Wei, Q.; Zhu, M.; Zheng, M.; Hou, Y. Giant strain of 0.65% obtained in B-site complex cations $(Zn_{1/3}Nb_{2/3})^{4+}$-modified BNT-7BT ceramics. *J. Alloys. Compd.* **2019**, *782*, 611-8. DOI
31. Ullah, A.; Ahn, C. W.; Hussain, A.; Lee, S. Y.; Lee, H. J.; Kim, I. W. Phase transitions and large electric field-induced strain in $BiAlO_3$-modified $Bi_{0.5}(Na, K)_{0.5}TiO_3$ lead-free piezoelectric ceramics. *Curr. Appl. Phys.* **2010**, *10*, 1174-81. DOI
32. Janbua, J.; Niemchareon, S.; Muanghlua, R.; Vittayakorn, N. High strain response of the $(1-x)(0.94Bi_{0.5}Na_{0.5}TiO_3$-$0.06BaTiO_3)$-$xBaSnO_3$ lead free piezoelectric ceramics system. *Ferroelectrics* **2016**, *490*, 13-22. DOI
33. Ge, R.; Zhao, Z.; Duan, S.; et al. Large electro-strain response of La^{3+} and Nb^{5+} co-doped ternary $0.85Bi_{0.5}Na_{0.5}TiO_3$-$0.11Bi_{0.5}K_{0.5}TiO_3$-$0.04BaTiO_3$ lead-free piezoelectric ceramics. *J. Alloys. Compd.* **2017**, *724*, 1000-6. DOI
34. Wang, C.; Lou, X. High energy storage properties of $0.94Bi_{0.5}Na_{0.5}TiO_3$-$0.06BaTiO_3$ ceramics by incorporating $Sr_{0.8}Bi_{0.1}\gamma_{0.1}Ti_{0.8}Zr_{0.2}O_{2.95}$. *Microstructures* **2023**, *3*, 2023023. DOI
35. Rahman, J. U.; Hussain, A.; Maqbool, A.; et al. Field induced strain response of lead-free $BaZrO_3$-modified $Bi_{0.5}Na_{0.5}TiO_3$-$BaTiO_3$ ceramics. *J. Alloys. Compd.* **2014**, *593*, 97-102. DOI
36. Cheng, R.; Xu, Z.; Chu, R.; Hao, J.; Du, J.; Li, G. Electric field-induced ultrahigh strain and large piezoelectric effect in $Bi_{1/2}Na_{1/2}TiO_3$-based lead-free piezoceramics. *J. Eur. Ceram. Soc.* **2016**, *36*, 489-96. DOI
37. Bafandeh, M. R.; Han, H.; Lee, J. Enhanced electric field induced strain in complex-ion Ga^{3+} and Ta^{5+}-doped 0.93BNT-0.07BT piezoceramic. *J. Electroceram.* **2021**, *47*, 89-99. DOI
38. Li, L.; Hao, J.; Xu, Z.; Li, W.; Chu, R.; Li, G. Large strain response in (Mn,Sb)-modified $(Bi_{0.5}Na_{0.5})_{0.935}Ba_{0.065}TiO_3$ lead-free piezoelectric ceramics. *Ceram. Int.* **2016**, *42*, 14886-93. DOI
39. Hao, J.; Xu, Z.; Chu, R.; Li, W.; Fu, P.; Du, J. Field-induced large strain in lead-free $(Bi_{0.5}Na_{0.5})_{1-x}Ba_xTi_{0.98}(Fe_{0.5}Ta_{0.5})_{0.02}O_3$ piezoelectric ceramics. *J. Alloys. Compd.* **2016**, *677*, 96-104. DOI
40. Schütz, D.; Deluca, M.; Krauss, W.; Feteira, A.; Jackson, T.; Reichmann, K. Lone-pair-induced covalency as the cause of temperature- and field-induced instabilities in bismuth sodium titanate. *Adv. Funct. Mater.* **2012**, *22*, 2285-94. DOI
41. Soergel, E. Piezoresponse force microscopy (PFM). *J. Phys. D. Appl. Phys.* **2011**, *44*, 464003. DOI
42. Jin, L.; Li, F.; Zhang, S.; Green, D. J. Decoding the fingerprint of ferroelectric loops: comprehension of the material properties and structures. *J. Am. Ceram. Soc.* **2014**, *97*, 1-27. DOI
43. Shannon, R. D. Revised effective ionic radii and systematic studies of interatomic distances in halides and chalcogenides. *Acta. Cryst. A.* **1976**, *32*, 751-67. DOI
44. Jing, R.; Chen, X.; Lian, H.; Qiao, X.; Shao, X.; Zhou, J. Comparative study on structure, dielectric, and piezoelectric properties of $(Na_{0.47}Bi_{0.47}Ba_{0.06})_{0.95}A_{0.05}TiO_3$ (A = Ca^{2+}/Sr^{2+}) ceramics: effect of radii of A-site cations. *J. Eur. Ceram. Soc.* **2018**, *38*, 3111-7. DOI
45. Pasha, U. M.; Zheng, H.; Thakur, O. P.; et al. *In situ* Raman spectroscopy of A-site doped barium titanate. *Appl. Phys. Lett.* **2007**, *91*, 062908. DOI
46. Zhang, Y.; Zeng, K.; Fu, J.; Xie, A.; Fu, Z.; Zuo, R. Giant strains of 0.70% achieved via a field-induced multiple phase transition in BNT-based relaxor antiferroelectric ceramics. *J. Eur. Ceram. Soc.* **2023**, *43*, 4748-56. DOI
47. Kreisel, J.; Glazer, A. M.; Bouvier, P.; Lucazeau, G. High-pressure Raman study of a relaxor ferroelectric: the $Na_{0.5}Bi_{0.5}TiO_3$ perovskite. *Phys. Rev. B.* **2001**, *63*, 174106. DOI
48. Kreisel, J.; Glazer, A. M.; Jones, G.; Thomas, P. A.; Abello, L.; Lucazeau, G. An X-ray diffraction and Raman spectroscopy investigation of A-site substituted perovskite compounds: the $(Na_{1-x}K_x)_{0.5}Bi_{0.5}TiO_3$ ($0 \leq x \leq 1$) solid solution. *J. Phys. Condens. Matter.* **2000**, *12*, 3267. DOI
49. Bokov, A. A.; Ye, Z. Recent progress in relaxor ferroelectrics with perovskite structure. *J. Mater. Sci.* **2006**, *41*, 31-52. DOI
50. Zhao, P.; Wang, H.; Wu, L.; et al. High-performance relaxor ferroelectric materials for energy storage applications. *Adv. Energy. Mater.* **2019**, *9*, 1803048. DOI
51. Li, G.; Ge, G.; Lin, J.; et al. Eco-friendly cooling materials with synergistic behavior of electromechanical and electrocaloric effects based on constructing B-site defect field. *Appl. Mater. Today.* **2022**, *26*, 101332. DOI
52. Jia, X.; Zhang, J.; Xing, H.; Wang, J.; Zheng, P.; Wen, F. Large electrostrain response in binary $Bi_{1/2}Na_{1/2}TiO_3$-$Ba(Mg_{1/3}Nb_{2/3})O_3$ solid solution ceramics. *J. Alloys. Compd.* **2018**, *741*, 7-13. DOI
53. Smolenskii, G. A. New ferroelectrics of complex composition. IV. *SciSpace* **1961**,. Available from: https://scispace.com/papers/new-ferroelectrics-of-complex-composition-iv-2wd1zsevvv [Last accessed on 7 Apr 2025]
54. Shi, J.; Zhao, Y.; He, J.; et al. Deferred polarization saturation boosting superior energy-storage efficiency and density simultaneously under moderate electric field in relaxor ferroelectrics. *ACS. Appl. Energy. Mater.* **2022**, *5*, 3436-46. DOI
55. Yin, J.; Zhao, C.; Zhang, Y.; Wu, J. Ultrahigh strain in site engineering-independent $Bi_{0.5}Na_{0.5}TiO_3$-based relaxor-ferroelectrics. *Acta. Mater.* **2018**, *147*, 70-7. DOI
56. Dong, G.; Fan, H.; Liu, L.; Ren, P.; Cheng, Z.; Zhang, S. Large electrostrain in $Bi_{1/2}Na_{1/2}TiO_3$-based relaxor ferroelectrics: a case study of $Bi_{1/2}Na_{1/2}TiO_3$-$Bi_{1/2}K_{1/2}TiO_3$-$Bi(Ni_{2/3}Nb_{1/3})O_3$ ceramics. *J. Materiomics.* **2021**, *7*, 593-602. DOI